TiH 2 -supported Ru catalyst with unusual electron transfer behaviour for highly efficient carbon dioxide methanation at low temperature

Zhujie He, Huanfeng Huang, Zhuodi Chen, Yuqian Liang, Zhixiang Huang, Shunlian Ning, Lilin Tan, Mihail Barboiu, Dawei Wang, Cheng-Yong Su

ARTICLE

TiH_2-supported Ru catalyst with unusual electron transfer behaviour for highly efficient carbon dioxide methanation at low temperature

Received 00th January 20xx,
Accepted 00th January 20xx

DOI: 10.1039/x0xx00000x

Zhujie He,[a] Huanfeng Huang,[a] Zhuodi Chen,[a] Yuqian Liang,[a] Zhixiang Huang,[a] Shunnian Ning,[a] Lilin Tan,[b] Mihail Barboiu, [a,c] Dawei Wang *[a] and Cheng-Yong Su [a]

Catalytic CO_2 methanation is of particular significance and growing interest due to its applications in many important industrial fields. The development of advanced heterogeneous catalysts for CO_2 methanation depends predominantly on the rational regulation of metal-support interaction (MSI), which remains challenging despite of recent progress. Here, we develop a new heterogeneous catalyst of TiH_2-supported Ru nanoparticles (NPs), which feature notable electron transfer from TiH_2 support to Ru NPs and enhanced capability of CO intermediate activation for CO_2 methanation, distinct from TiO_2-supported Ru catalysts synthesized under similar mild conditions. The electron transfer behavior and hydrogen spillover effect in TiH_2-supported Ru NPs (denoted as RTH) are optimized at a moderate Ru loading of 9.8 wt.% in 100RTH, where the impacts of Ru loading on CO intermediate activation, H_2 activation and catalyst surface hydration are synergistically balanced. When evaluated at 200 °C under 4 bar pressure, 100RTH delivers a notable CH_4 selectivity of 99.8% and a superior CH_4 production rate of 168.7 mmol h^{-1} g_{Ru}^{-1}, which is 21.1 times more active than pure Ru NPs. Our work provides valuable insights into the MSI-directed development of heterogeneous catalysts for highly efficient CO_2 conversion and utilization.

Introduction

The excess emission of carbon dioxide (CO_2), the primary greenhouse gas, have caused challenging issues including global warming, biological system imbalances, and ocean acidification in the past decades.[1, 2] It is therefore highly desirable to develop capable technology and devices for efficient capture, utilization, and storage of CO_2. As a promising strategy to achieve net-zero emission fuel cycle, catalytic CO_2 hydrogenation have attracted extensive interest, since it allows the conversion of CO_2 into various value-added chemicals such as CO, CH_4, CH_3OH, HCOOH, and other hydrocarbons.[2, 3] The catalytic hydrogeneration of CO_2 to produce CH_4 (known as CO_2 methanation or Sabatier reaction) are of particular significance and growing interest in recent years, which has found applications in several important industrial fields including the production of synthetic nature gas and the hydrogen feedstock purification for ammonia production.[4, 5] Due to the strong C=O double bonds of CO_2 (bond energy of 750 kJ mol^{-1}),[6] CO_2 methanation process is usually operated at high temperature (>300 °C) and in the presence of heterogeneous catalysts. Typical heterogeneous catalysts for CO_2 methanation are highly active metal nanoparticles (NPs; such as Ru, Rh, Co, and Ni[7-14]) supported on reducible oxide supports (like TiO_2, CeO_2, and ZrO_2[7, 8, 13, 15, 16]) that anchor metallic NPs and prevent NPs from agglomeration at high reaction temperature. For such heterogeneous catalysts, the metal–support interaction (MSI) has a critical impact on the physiochemical properties of catalysts and the catalytic hydrogeneration process.[17, 18] Rational MSI regulation thus has been widely used as a predominant strategy to achieve excellent catalytic performance (activity, selectivity, and stability) for CO_2 hydrogeneration.

Typical MSI operating in catalytic CO_2 hydrogeneration includes electron transfer, strong metal-support interaction (SMSI), and hydrogen spillover.[7] Taking supported Ru catalyst, one of the most efficient heterogeneous catalysts towards CO_2 hydrogeneration, for an example, recent studies reveal that the support–metal electron transfer plays a crucial role in the product selectivity, by impacting on the adsorption and activation of CO intermediates.[16, 19, 20] Due to the partially positive charge on the C atoms of C=O bonds in CO intermediates, electron transfer from Ru to TiO_2 decreases the electron density around Ru NPs and thus moderately weakens the adsorption and subsequent activation of CO intermediates on Ru, leading to high CO selectivity over CH_4.[20] In contrast, electron transfer from CeO_2 support to Ru increases the electron density around Ru NPs, which facilitates the adsorption and activation of CO intermediates and in turn results in 100% CH_4 selectivity.[16] SMSI is usually observed when reducible oxides (e.g., TiO_2) are used as support for metal NPs and (partially) reduced at high temperature (300–700 °C) under

[a] Lehn Institute of Functional Materials, MOE Laboratory of Bioinorganic and Synthetic Chemistry, School of Chemistry, Sun Yat-Sen University, Guangzhou 510275, China. E-mail: wdawei@mail.sysu.edu.cn
[b] Chemistry and Chemical Engineering Guangdong Laboratory, Shantou 515031, China
[c] Institut Europeen des Membranes, Adaptive Supramolecular Nanosystems Group, University of Montpellier, ENSCM-CNRS, Place E. Bataillon CC047, 34095 Montpellier, France
Electronic Supplementary Information (ESI) available. See DOI: 10.1039/x0xx00000x

reducing atmosphere (typically, H_2) or ultrahigh vacuum, leading to the migration of support to metal NP surface and the subsequent formation of an oxide overlayer around metal NPs.[9, 21] For TiO_2-supported Ru catalysts, SMSI generally results in deteriorative activity but enhanced stability of Ru NPs due to the coverage of their surface sites by TiO_2 overlayer.[7] Moreover, due to the higher Fermi lever of partially reduced TiO_2 support as compared with Ru NPs, SMSI induces electron transfer from TiO_2 support to Ru NPs and thus results in high CH_4 selectivity,[7, 22, 23] in sharp contrast to TiO_2-supported Ru catalysts prepared under mild conditions (e.g., wet impregnation method), in which the electron transfer from Ru to TiO_2 leads to high CO selectivity.[20]

Hydrogen spillover also readily occurs when reducible oxide supported metal NP catalysts are used for CO_2 hydrogenation. Hydrogen spillover benefits the activation of H_2, since abundant, highly active hydrogen atoms can be generated by the dissociative adsorption of H_2 on metal NP surfaces and the spontaneous migration of hydrogen atoms to the surface of reducible oxide support.[21] Therefore, hydrogen spillover has been been utilized to improve the activity of supported catalysts towards CO_2 hydrogenation. However, recent study based on CeO_2-supported Ru catalysts reveals that hydrogen spillover should be regulated at an appropriate level to suppress the adverse hydration of catalyst surfaces, and also to achieve a balance with SMSI due to their competitive relationship.[16] Given the critical and complex roles of MSI in the performances of supported catalysts, the rational regulation of MSI is therefore of notable significance for highly efficient CO_2 methanation, which remains very challenging despite recent progresses.[17, 24]

Here, we develop a new heterogeneous catalyst for CO_2 methanation, by utilizing TiH_2 as the support for Ru NPs. TiH_2-supported Ru NPs (denoted as *m*RTH, in which *m* refers to the mass loading of $RuCl_3$ precursor in mg) can be readily prepared in solution by the deposition of Ru NPs on TiH_2. Benefitting from the highly active, negatively charged hydrogen species of H^- in TiH_2, spontaneous oxidation of TiH_2 surface occurs under ambient conditions,[25] leading to the formation of a thin surface layer of oxides and oxyhydrides (denoted as TiO_xH_y) between bulk TiH_2 and Ru NPs. The TiO_xH_y surface layer acts as partially reduced oxide support for Ru NPs and enables notable electron transfer from support to Ru NPs, which thus remarkably enhances the activation of CO intermediates on Ru NPs, and in turn results in superior activity and CH_4 selectivity towards catalytic CO_2 methanation. Despite similar electron transfer behaviour observed in SMSI-mediated TiO_2-supported Ru catalysts, the TiH_2-supported Ru NPs do not require reduction treatment at very high temperature (300–700 °C), and thus avoids the formation of adverse oxide overlayer on Ru NPs that impairs the catalytic activity and/or selectivity of Ru NPs. Moreover, such electron transfer behaviour has not been observed in traditional TiO_2-supported Ru catalysts synthesized under similar mild conditions, in which the electron transfer from Ru to TiO_2 results in high CO selectivity. Additionally, the electron transfer is appropriately coupled with hydrogen spillover effect to achieve synergistic balance between CO activation, H_2 activation and catalyst surface hydration, which finally imparts superior activity and CH_4 selectivity to TiH_2-supported Ru NPs for catalytic CO_2 methanation.

Experimental

Chemicals

Ruthenium trichloride ($RuCl_3$) was purchased from Bide Pharmatech Ltd. Titanium hydride (TiH_2, 95%; >99% Ti) was purchased from Strem Chemicals Inc. Ethyl Glycol (99.5%) was purchased from Titan Scientific Company Ltd, Shanghai. Millipore deionized water (18.2 MΩ·cm) was used for solution preparation. All reagents were used as received unless otherwise noted.

Synthesis of *m*RTH (*m* = 50, 100, 150, and 200)

TiH_2 powder (200 mg) was added to a round bottom flask (100 mL) with ethylene glycol (EG; 25 mL) and deionized water (25 mL), and treated with ultrasonication and vigorous stirring for 15 min. Then $RuCl_3$ (50 mg) were added to the solution, and treated with ultrasonication and vigorous stirring for 60 min. Subsequently, the obtained brownish-black solution was heated at 150 °C with an oil bath for 180 min, and allowed to cool down to room temperature under ambient condition. The product, denoted as 50RTH, was collected by centrifugation and washed with water and ethanol three times. The synthesis of other samples of 100RTH, 150RTH, and 200RTH was achieved by changing the mass of $RuCl_3$ while keeping all the other parameters unchanged.

Synthesis of Ru NPs

The synthesis of Ru NPs (as control sample) was accomplished by following the same procedure for the synthesis of Ru NPs described above. Briefly, RuCl3 (50 mg) were added to a round bottom flask (100mL) with EG (25 mL) and deionized water (25 mL) under 15 min of ultrasonication and vigorous stirring, and heated at 150 °C with an oil bath for 180 min. After cooling down the solution to room temperature, the product was collected by centrifugation and washed three times with water and ethanol.

Characterization

The powder X-ray diffraction (PXRD) patterns were collected with a Rigaku MiniFlex 600 X-ray diffractometer (Cu Kα). The morphology of samples was recorded with a field-emission scanning electron microscope (FE-SEM, Hitachi, SU8010) operated at 5 kV and 10 mA. The transmission electron microscopy (TEM) and high-resolution TEM (HRTEM) images and energy-dispersive X-ray spectroscopy (EDX) data were recorded with a spherical aberration corrected transmission electron microscope (SAC-TEM, JEM-ARM200P) operated at 200 kV. The chemical states of elements were probed by X-ray photoelectron spectroscopy (XPS, Thermo Fisher Nexsa). The surface profile and potential were obtained with an atomic force microscope (AFM) and Kelvin probe force microscope (KPFM; Bruker Dimension Fastscan). The precise element composition was detected with an inductively coupled plasma-

emission spectrometer (ICP-OES) equipped with an Agilent 5110 spectrometer. Diffuse reflectance infrared Fourier transform spectroscopy (DRIFTS) were conducted on a Thermo Scientific Nicolet iS20 spectrometer.

The hydrogen spillover effect was investigated by temperature-programmed reduction (TPR) with a chemisorption analyser (BELCAT II, MicrotracBEL). Before TPR test, samples (51 mg) were heated to 100 °C at a ramp rate of 10 °C min^{-1}, kept at 100 °C for 30 min to remove adsorbed H_2O, and cooled to 50 °C under nitrogen atmosphere. Then the samples were kept for 60 min in 10% H_2–90% N_2 flow at a flow rate of 30 mL min^{-1}. Finally, the samples were heated to 900 °C at a ramp rate of 5 °C min^{-1} in a 10% H_2–90% N_2 flow at a flow rate of 30 mL min^{-1}.

Catalytic CO_2 hydrogenation

The catalytic performances of *m*RTH for CO_2 hydrogenation were evaluated with a commercial evaluation system (CEL-HPR100T+, Beijing China Education Au-Light Co., Ltd). Typically, catalyst powder (40 mg) was placed in a quartz cup (150 mL) that was sealed within stainless steel and transferred into an autoclave. A CO_2/H_2 mixture (CO_2:H_2 = 1:4; 4 bar) was filled in the autoclave after evacuation for several times, and allowed to proceed at 200 °C. The products were detected with a gas chromatography (FL 9790) equipped with a flame ionization detector and thermal conductivity detector.

Results and discussion

*m*RTH were prepared by a wet synthesis procedure, using EG as reductant (cf. Experimental for details). As presented in the typical SEM and TEM images in Fig. 1a and S1, TiH_2 are large particles with size of around 2–10 μm, which show a lattice spacing of 2.58 Å corresponding to the (111) lattice plane of cubic TiH_2.[25, 27-29]. Each microscale TiH_2 particle is coated with Ru NPs of around 3 nm in average diameter, to form *m*RTH with hybrid structure (Fig. 1b–d). Interesting, the Ru NPs exist in the form of large aggregates of 30-100 nm in diameter (Fig. 1c & Fig. 2a–g), which is likely due to the aggregation of adjacent Ru NPs induced by van der Waals interactions.[30, 31] Each small Ru NP in large Ru aggregates can be identified in HRTEM image (Fig. 1d), which shows a lattice spacing of 2.03 Å corresponding to the (101) plane of Ru with hexagonal crystalline structures.[32] The EDX element maps of *m*RTH (*m* = 100 in Fig. 1e; *m* = 50, 150, and 200 in Fig. 2h–j, respectively) confirm the elemental composition of Ru and Ti in the samples, and the precise content of Ru and Ti is determined by ICP-OES (Table S1), which gives a a Ru loading of 5.7, 9.8, 15.5, and 17.3 wt % in 50-, 100-, 150-, and 200RTH, respectively. The appearance of O in the EDX elemental maps should be attributed to the formation of TiO_xH_y layer on the surface of TiH_2, which is induced by the oxidation of TiH_2 by atmospheric oxygen under ambient conditions.[33, 34] The PXRD patterns of *m*RTH show a set of peaks centred at 34.9, 40.5, 58.6, 70.1, and 73.7°, respectively, which is indexed to cubic TiH_2 (PDF #07-0370). By contrast, the PXRD peaks of hexagonal Ru (PDF #06-0663) located at 44.0° are only visible in the *m*RTH samples with high Ru loading in 100-, 150-, and 200RTH; the PXRD peaks of Ru in 50RTH samples is almost invisible, likely due to the low loading of Ru NPs with small size (*ca*. 3 nm).[35-38] The PXRD patterns, together with the TEM images and EDX element maps, thus collectively verify the hybrid Ru/TiH_2 structure of *m*RTH.

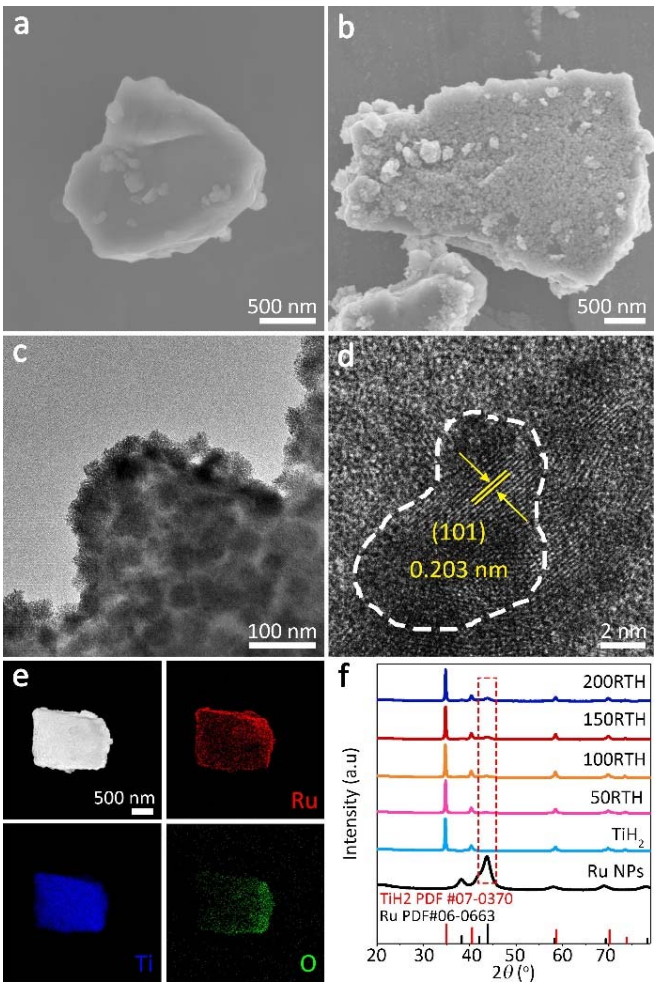

Fig. 1 (a) SEM image of TiH_2. (b) SEM, (c) TEM, and (d) HRTEM images of 100RTH. (e) EDX element maps of 100RTH. (f) PXRD patterns of *m*RTH, TiH_2 and Ru NPs.

It is worth noting that the spatial dispersion of Ru NPs in *m*RTH relates closely to Ru loading (Fig. 2). As the Ru loading increases, Ru NPs organize into discrete aggregates in 50RTH (5.7 wt %), a dense layer of Ru NP aggregates in 100RTH (9.8 wt %), a dense Ru NP aggregate layer with excess Ru aggregates in 150RTH (15.5 wt %), and dense double aggregate layers in 200RTH (17.3 wt %); meanwhile, the size of Ru NP aggregates in 100-, 150- and 200RTH is comparable (*ca*. 52 nm), while the size of Ru NP aggregates in 50RTH is smaller (*ca*. 38 nm) due to the low surface coverage of Ru NPs on TiH_2 (cf. Fig. 1b–d and Fig. 2b–g). Moreover, all the Ru NP aggregates are in direct contact with TiH_2 in 50- and 100RTH. In contrast, only the first Ru NP aggregate layer is in direct contact with TiH_2, while the other Ru NP aggregates are separated by the first Ru layer in 150- and 200RTh. Such differences in the surface coverage, size, and spatial organization of Ru NP aggregates leads to the varied interfacial structure of *m*RTH, which in turn, as demonstrated later in this work, have critical impact on the MSI (interfacial

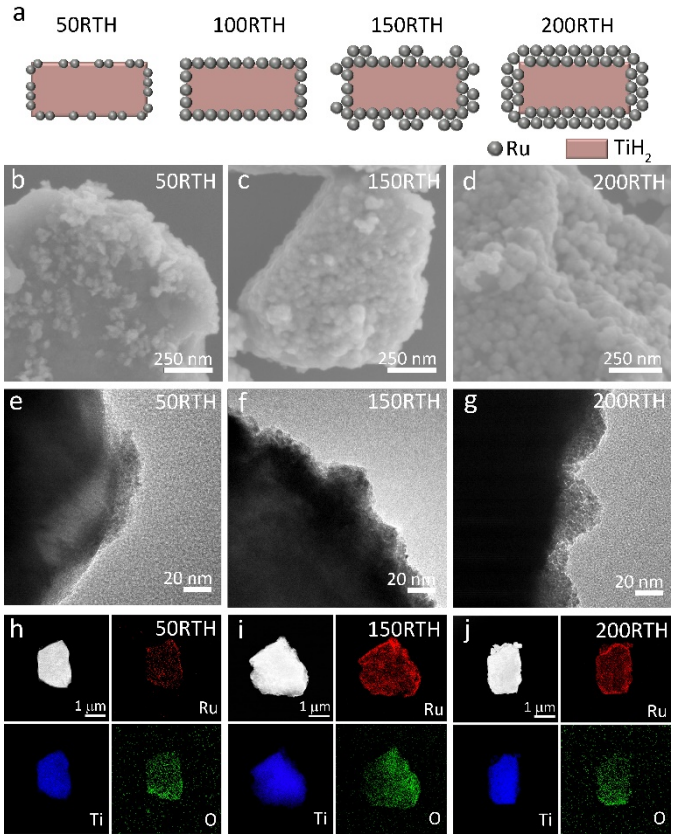

Fig. 2 (a) Schematic illustration of spatial dispersion of *m*RTH with increasing Ru loading. (b–d) SEM and (e–g) TEM images, and (h–j) EDX element maps of *m*RTH (*m* = 50, 150, and 200). cf. the data for 100RTH in Fig. 1b–e.

electron transfer and hydrogen spillover) and the consequent catalytic activity of *m*RTH towards CO_2 methanation.

The MSI between Ru NPs and TiH_2 were systematically investigated by AFM coupled with KPFM, XPS, and H_2-TPR. AFM-KPFM was first used to investigate the charge transfer behaviour in *m*RTH. By selecting single particle of TiH_2 and *m*RTH (Fig. 3a–e), the typical surface potential of TiH_2 and *m*RTH can be obtained and compared by contact potential difference (CPD) given by CPD = $E_{sample} - E_{substrate}$, where E_{sample} and $E_{substrate}$ are the measured surface potential of sample and substrate, respectively, and *n*–Si(111) was used as the substrate for our KPFM measurements (Fig. 3f–j and Table S2).[39, 40] The CPD shows a positive corelation with the Ru loading in sample, increasing from –8 mV for TiH_2, to 2 mV for 50RTH, 26 mV for 100RTH, 37.4 mV for 150RTH, and 68.8 mV for 200RTH. The CPD shift from negative (TiH_2) to positive (*m*RTH) values confirms the electron transfer from TiH_2 to Ru NPs.[41] Moreover, due to the positive correlation between CPD and Fermi level, 50RTH with the lowest positive CPD should have the lowest Fermi level among all *m*RTH, which thus should allow for the easiest electron transfer from TiH_2 to Ru NPs.[40]

To obtain more details about the interfacial electron transfer and the chemical states of interface species in *m*RTH, XPS spectra were collected. For TiH_2 and *m*RTH, the high-resolution XPS spectra of Ti $2p_{3/2}$ and Ru $3d_{5/2}$ indicate that in all samples the surface Ti species exist in the forms of Ti^{4+} and defective TiO_{2-x} in the TiO_xH_y surface layer (Fig. 4a; cf. Table S3 for the binding energy corresponding to each peak), and Ru exists in the form of Ru^0 and Ru^{4+} (Fig. 4b).[27, 28, 33, 34, 42, 43] The formation of TiO_{2-x} and Ru^{4+} is induced by the spontaneous oxidation of TiH_2 and Ru surfaces by atmospheric oxygen under ambient conditions,[7, 34, 43, 44] which agrees well with the results of EDX element maps shown in Fig. 1e. Moreover, as compared with TiH_2, the *m*RTH samples show increasing binding energies of Ti^{4+} and defective TiO_{2-x}, and the binding energy shifts increase steadily from 50RTH to 200RTH. In contrast, the *m*RTH samples present decreasing binding energies of Ru^0 and Ru^{4+} as compared with Ru NPs, and the absolute binding energy shifts decrease steadily from 50RTH to 200RTH (Fig. 4b). Such opposite binding energy shift trends in TiH_2 and Ru NPs imply interfacial electron transfer from TiO_xH_y to Ru, which agrees well with our KPFM results (Fig. 3) and thus confirms the MSI in *m*RTH. Notably, the interfacial electron transfer from TiO_xH_y to Ru results in the formation of electron-enriched Ru species ($Ru^{\delta-}$) in *m*RTH. As demonstrated later in this work, the Ru species are the dominate sites for CO_2 absorption; moreover, electron-enriched Ru species could benefit the chemisorption of CO_2 and the formation of $[O=C=O]^{\delta-}$ intermediates, and thus efficiently accelerate the CO_2 methanation reaction. It is worth noting that

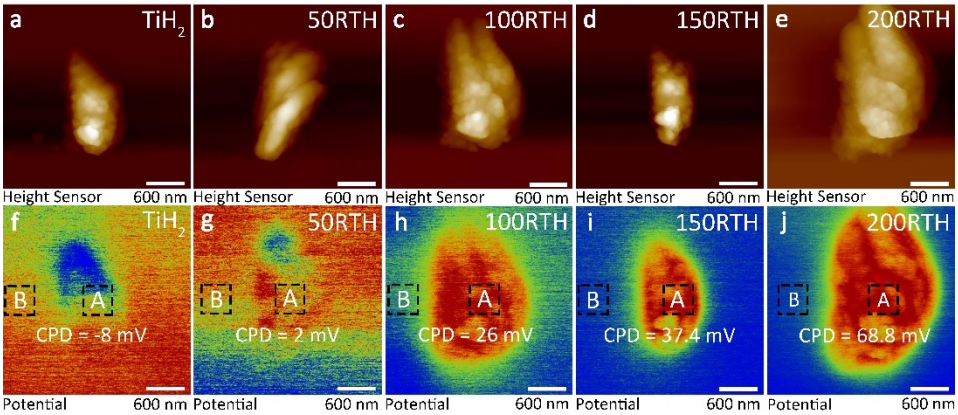

Fig. 3 (a–e) AFM height images and (f–j) the corresponding KPFM potential profiles of TiH_2 and *m*RTH. (a, f) TiH_2, (b, g) 50RTH, (c, h) 100RTH, (d, i) 150RTH, and (e, j) 200RTH. CPD in (f–j) is estimated by the potential difference between site A (sample) and B (substrate).

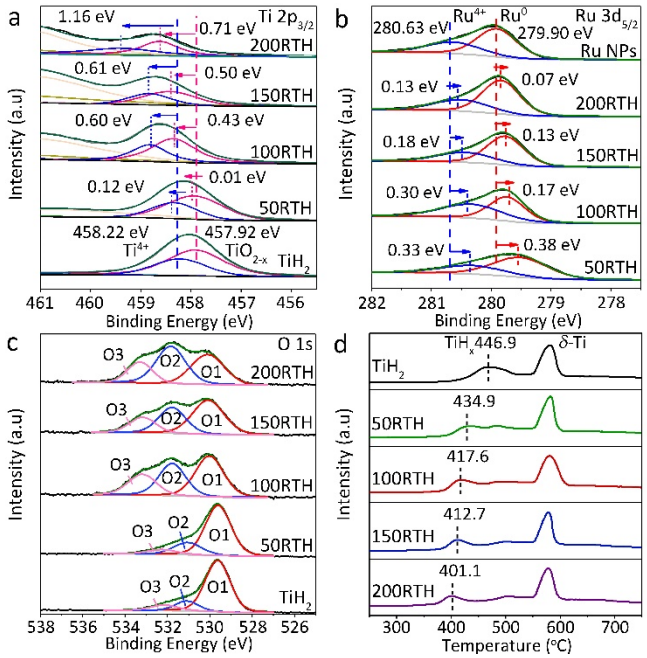

Fig. 2 (a–c) High-resolution XPS spectra of Ru NPs, TiH_2, and *m*RTH, (a) Ti $2p_{3/2}$, (b) Ru $3d_{5/2}$, and (c) O 1s. (d) H_2-TPR profiles of TiH_2 and *m*RTH.

the interfacial electron transfer from TiO_2 to metal NPs (e.g., Ru,[7] Pt,[25] and Ni[45]) typically occurs in the case of SMSI, which is induced by the partial reduction of TiO_2 support when treated at high-temperature (typically, >300 °C) and under H_2 atmospheres. In contrast, for the TiO_2-supported metal NPs (e.g., Ru[20] and Au[46]) prepared under mild conditions that disfavour support reduction, the electron transfer usually occurs in opposite direction, that is, from metal NPs to TiO_2. Therefore, the unusual charge transfer from TiO_xH_y to Ru NPs in our *m*RTH prepared under mild condition (wet synthetic process; see details in Experimental) should be attributed to the highly active, negatively charged H^- in TiH_2, which leads to the spontaneous oxidation of TiH_2 surface into TiO_xH_y layer consisting of oxides and oxyhydrides (cf. Ref. 23 and also the Ti $2p_{3/2}$ and O 1s XPS spectra in Fig. 4), and thus enables the TiO_xH_y surface layer to acts as partially reduced oxide support for Ru NPs, similar to the role of TiO_2 partially reduced at high-temperature and under H_2 atmospheres in the case of SMSI.

To rationalize the opposite impact of Ru loading on the peak shifts in the Ti $2p_{3/2}$ and Ru $3d_{5/2}$ XPS spectra of *m*RTH, the spatial dispersion of Ru NPs on TiH_2 has to be taken into account. Note that the XPS spectra are collected based on a typical spot size of 30–500 μm, much larger than the size of all *m*RTH samples (< 5 μm; cf. Fig. 1–2), the XPS peak position could be regarded as a rough indicator of the binding energy averaged over all the surface Ti or Ru species, in which the surface Ti species could be estimated to be the same for all *m*RTH and the surface Ru species reply specifically on the Ru loading in each *m*RTH. Generally, increasing Ru loading leads to raised surface density of Ru NP aggregates that interact with the surface layer of TiH_2, and accordingly enhanced overall MSI at the interface. In such a way, the MSI shows increasing impact on the binding energy of the surface Ti species of TiH_2 (approximately the same for all *m*RTH), and thus the Ti $2p_{3/2}$ XPS peaks continuously shift upwards as the Ru loading in 50-, 100-, 150- and 200RTH steadily increases (Fig. 4a). Notably, 100RTH presents much more remarkable shift of the Ti $2p_{3/2}$ XPS peak position than 50RTH, which could be attributed to the much greater surface density of Ru NP aggregates in 100RTH (9.8 wt %; vs. 5.7 wt % in 50RTH). Moreover, the Ru NP aggregates in the second layer of 150- and 200RTH are in indirect contact with the surface layer of TiH_2, and thus are less efficiently involved in MSI as compared with the Ru NP aggregates in the first layer that are in direct contact with the surface layer of TiH_2. Although the overall MSI shows a rising trend as the Ru loading in 100-, 150- and 200RTH steadily increases, the overall MSI averaged over all the surface Ru species are declining, thus having a decreasing impact on the binding energies of surface Ru species and leading to downward shifts in the Ru $3d_{5/2}$ XPS peak position (Fig. 4b). Moreover, in the case of 50- and 100RTH with all the Ru NP aggregates in direct contact with the surface layer of TiH_2, the notable shift in the Ru $3d_{5/2}$ XPS peak of 50RTH is likely due to the smaller size of Ru NP aggregates in 50RTH (38 nm; vs. 52 nm for 100RTH), which results in much stronger MSI and consequently much greater impact on the binding energies of Ru species in 50RTH.

The O 1s spectra of *m*RTH and TiH_2 are also analysed. As shown in Fig. 4c, all the O 1s spectra show three types of O species that correspond to the lattice O in TiO_xH_y and RuO_2 (denoted as O1), the O at defect (oxygen vacancy) sites or Ti–OH (O2), and the O in chemically adsorbed oxygen-containing species like H_2O (O3).[25, 33] The appearance of O1 and O2 peaks confirms the partial oxidation of surface TiH_2 resulted from the highly active nature of the negatively charged H^- in TiH_2. Moreover, the Ru loading in *m*RTH correlates with greater integrated peak areas of O2 and O3, which is likely due to the low migration energy of H^- at the Ru–metal hydride interface.[26] Briefly, the low migration energy favors the migration of H^- from TiH_2 to the Ru, and higher Ru loading thus allows for the formation of more oxides and oxyhydrides of Ti through ambient oxidation of H^- at the interface, and gives rise to the increased peak areas of O2. Both the oxygen vacancy and OH group in TiO_xH_y surface layer have good binding affinity to H_2O under ambient conditions,[47, 48] thus leading to enhanced adsorption of H_2O and increased peak area of O3 at higher Ru loading level.

H_2-TPR was also used to further evaluate the Ru–TiH_2 MSI as well as the reducibility of TiH_2 support.[49] As presented in Fig. 4d, all the H_2-TPR profiles of TiH_2 and *m*RTH show two H_2 consumption peaks in the temperature range of 250–750 °C, one centred in the range of 400–450 °C corresponding to the hydrogen storage by β-TiH_x phase in TiH_2, and the other centred at 580 °C corresponding to the hydrogen storage by α-Ti phase in TiH_2.[50-53] The later peaks locate at almost the same temperature for TiH_2 and *m*RTH, in agreement with the results reported in literature.[25] In contrast, the former peaks related to the reduction of TiO_xH_y surface layer and bulk TiH_2 shift towards lower temperature when the Ru loading in *m*RTH increases, indicating improved reducibility of TiH_2 by Ru loading. The improved reducibility of TiH_2 could be interpreted as a consequence of Ru–TiH_2 MSI. Specifically, as implied by the XPS

spectra in Fig. 4a–c, the charge transfer from TiH_2 to Ru increases the electron density at the Ru–TiH_2 interface, and thus enables the surface TiO_xH_y layer to be partially reduced at a lower temperature. Moreover, H_2 could be remarkably activated by TiO_xH_y-supported Ru NPs through hydrogen spillover effect[54-56], and oxygen vacancies on TiO_xH_y-support could further enhance the hydrogen spillover effect by facilitating the transfer of active hydrogen species,[57] thus further enhancing the reducibility of TiH_2. As both the Ti–Ru charge transfer behaviour and the hydrogen spillover effect are positively related to the Ru loading (abundant active hydrogen species can be generated by more Ru NPs), 200RTH with the highest Ru loading shows notable decrease, from 469.7 to 401.1 °C, in the peak temperature for the reduction of TiH_2.

The catalytic performances of *m*RTH towards CO_2 methanation were evaluated at 200 °C and in an autoclave filled with 4 bar of reaction gas of stoichiometric ratio (20 vol.% CO_2 and 80 vol.% H_2). Control experiments using TiH_2 support and Ru NPs as catalysts were also conducted under otherwise identical conditions. Approximately, the conversion of CO_2 with representative catalysts (TiH_2, Ru NPs, and 100RTH; Fig. 5a) increases linearly with reaction time, which shows a typical feature of heterogeneous catalysis occurring on the catalyst surface and implies a reaction kinetics depending primarily on the surface properties of catalysts. An overall comparison of CO_2 conversion and CH_4 selectivity between TiH_2, Ru NPs, and *m*RTH are presented in Fig. 5b. Despite notable difference in CO_2 conversion, all the TiH_2, Ru NPs, and *m*RTH show superior CH_4 selectivity of >99.4%. Moreover, all *m*RTH show remarkably improved conversion (44.7, 86.5, 72.8, and 61.0% for 50-, 100-, 150-, and 200RTH, respectively) as compared with Ru NPs (29.0%) and TiH_2 (1.2%), which thus indicates notable synergistic effect between TiH_2 and Ru. The superior selectivity and activity towards CO_2 methanation demonstrates the advantages of *m*RTH over traditional Ru–TiO_2 heterogeneous catalyst prepared under similar mild conditions and SMSI-mediated Ru–TiO_2 heterogeneous catalysts synthesized by high-temperature reduction.[8, 20] As compared with the former one, *m*RTH show superior selectivity and activity towards CH_4 production, resulting from the usual electron transfer from TiO_xH_y surface layer to Ru NPs that leads to the generation of electron-enriched Ru NPs with enhanced activation capability for CO intermediates. As compared with the later one, the superior activity of *m*RTH could be attributed to the efficiently exposed Ru NPs, whose activity are otherwise largely impaired due to the coverage of adverse oxide overlayers in SMSI-mediated Ru–TiO_2 heterogeneous catalysts.

A more accurate comparison of the catalytic activities between TiH_2, Ru NPs, and *m*RTH was made based on specific activities, which are indicated by the reaction rate of CH_4 with respect to the total catalyst mass (denoted as $r(CH_4, Cat.)$) or the mass of Ru in each catalyst (denoted as $r(CH_4, Ru)$), respectively (Fig. 5c). Given the same mass of catalysts used in CO_2 methanation, the trend in $r(CH_4, Cat.)$ is, as expected, in line

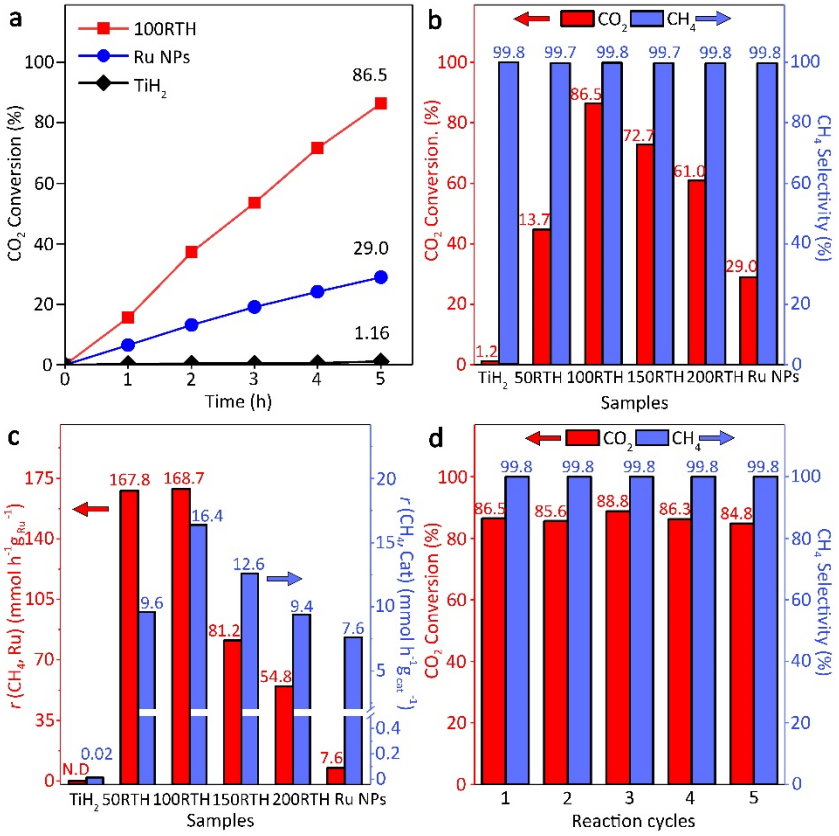

Fig. 3 Reaction kinetics of catalytic CO_2 methanation and catalyst stability. (a) Typical CO_2 conversion curves as a function of reaction time. (b) CO_2 conversion and CH_4 selectivity after 5 h of reaction. (c) Reaction rate of CH_4 with respect to catalyst mass and Ru mass in catalyst, (d) Catalyst stability of 100RTH.

with the trend in CO_2 conversion. However, $r(CH_4, Ru)$ shows two different features: (1) impressively, 50-, 100, 150-, and 200RTH delivers a large $r(CH_4, Ru)$ of 167.8, 168.7, 81.2 and 54.8 mmol h^{-1} g_{Ru}^{-1}, which is 21.0, 21.1, 9.6, and 6.2 times higher than that of Ru NPs (7.6 mmol h^{-1} g_{Ru}^{-1}), respectively, and thus implies that the catalytic activity of Ru NPs can be remarkably enhanced by TiH_2 support; (2) 50- and 100RTH with low loading of Ru NP aggregates in direct contact with TiH_2 surface show very comparable $r(CH_4, Ru)$ of 167.8 and 168.7 mmol h^{-1} g_{Ru}^{-1}, respectively, which are both much higher than 150- and 200 RTH with high loading of Ru NP aggregates in both direct and indirect contact with TiH_2 surface. The two features of $r(CH_4, Ru)$ clearly indicate that the Ru-TiH_2 interface could substantially increase the catalytic activity of Ru, and direct Ru-TiH_2 contact induces much more efficient interface for boosting the catalytic activity of Ru than indirect Ru-TiH_2 contact. These results thus confirm and highlight the critical role of appropriate Ru-TiH_2 MSI on the catalytic activity of *m*RTH towards CO_2 methanation, which will be discussed in detail later in this work. Moreover, despite comparable specific activity of Ru NPs in 100RTH and 50RTH, 100RTH is selected as the optimum catalyst for CO_2 methanation, due to its higher Ru loading that benefits more efficient utilization of TiH_2 (indicated by higher $r(CH_4, Cat.)$). It is also worth noting that catalytic activity of 100RTH, indicated by its $r(CH_4, Ru)$ up to 168.7 mmol h^{-1} g_{Ru}^{-1}, is superior to most of the Ru-based heterogeneous catalysts reported in literature, and thus enables 100RTH to be among the best Ru-based heterogeneous catalysts for CO_2 methanation, particular those working efficiently at temperature ≤200 °C (cf. Table S4).

The stability of *m*RTH was also evaluated. Taking 100RTH for instance, the CO_2 conversion and CH_4 selectivity show neglectable change even after 5 cycles (equivalently, 25 h; Fig. 5d) of successive operation, which thus demonstrates its excellent cycling stability.

To get insights into the excellent catalytic activity of 100RTH and the activity differences between various *m*RTH, two important control experiments were adequately designed and conducted, and TiH_2, Ru, and 100RTH were selected as representative catalysts. The first one was the sorption of CO_2 on catalyst surfaces, in which CO_2 was first allowed to be adsorbed on catalyst surface at 30 °C for 30 min, and then desorbed at elevated temperature (5 °C min^{-1}) in N_2 flow (50 mL min^{-1}). The whole sorption processes were monitored with *in situ* DRIFTS. As shown in Fig. 6a–c, the DRIFTS spectra of TiH_2, Ru, and 100RTH all show absorption peaks at 1640 cm^{-1}, which is attributed to the adsorbed CO_2 species of $[O=C=O]^{\delta-}$ on catalyst surface.[60-62] However, the sorption peaks at 1640 cm^{-1} in the spectra of Ru NPs and 100RTH are much more intense than the corresponding peaks of TiH_2 at the same temperature. Moreover, another sorption peaks can also be found at ca. 2100 cm^{-1} in the enlarged DRIFTS spectra of Ru NPs and 100RTH, which correspond to $Ru(CO)_n$ species generated by the partial dissociation of adsorbed CO_2 on Ru NP surfaces.[7, 63, 64] The peaks of $Ru(CO)_n$ species, however, are not found in the spectra of TiH_2. Such different sorption behaviour between TiH_2, Ru, and 100RTH revealed by DRIFTS spectra thus indicates that Ru NPs have much stronger CO_2 adsorption affinity than TiH_2, and the Ru NPs in 100RTH are the predominant sites for CO_2 adsorption. Moreover, it is of particular interesting to note that Ru NPs and 100RTH show significantly different development trend of the $Ru(CO)_n$ peaks at elevated temperature. As the temperature increases from 30 to 200 °C, the $Ru(CO)_n$ peaks of Ru NPs

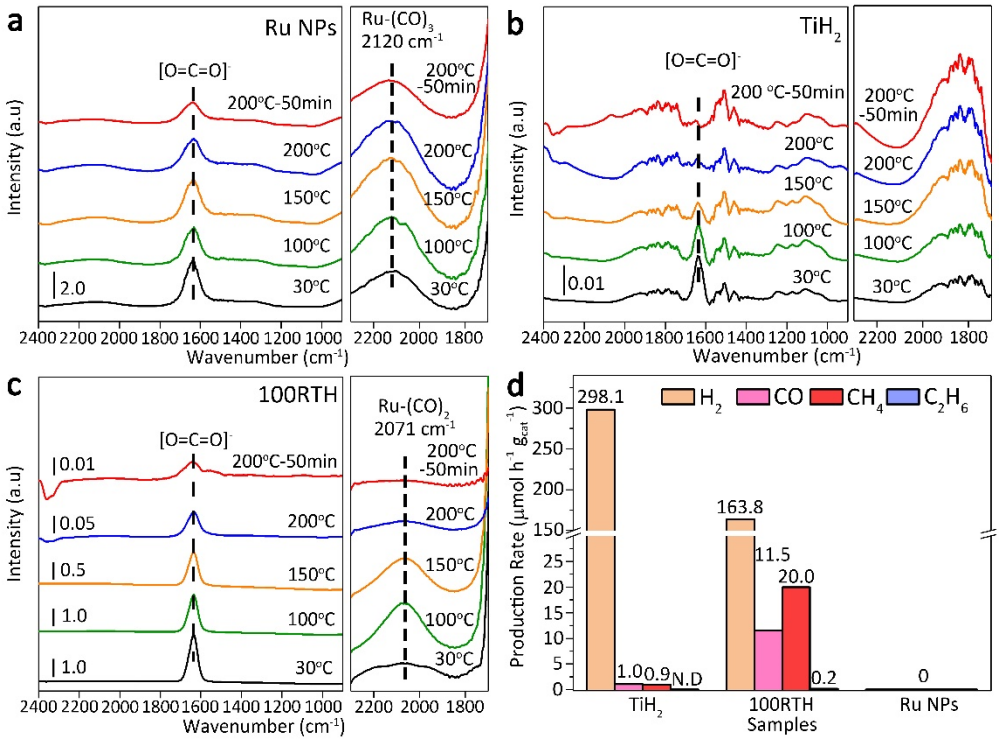

Fig. 4 (a–c) *In situ* DRIFTS spectra of CO_2 sorption on (a) Ru NPs, (b) TiH_2, and (c) 100RTH at varied temperature. (d) Reaction rate of catalytic CO_2 methanation in the absence of external H_2.

roughly remain their intensity; in sharp contrast, the $Ru(CO)_n$ peaks of 100RTH decline rapidly in their intensity and even vanishes after keeping 100RTH at 200 °C for 50 min. As revealed below, hydrogen stored in TiH_2 can be released at elevated temperature (Fig. 6d). The rapid declined peak intensity of $Ru(CO)_n$ in 100RTH thus should be attributed to the reduction of adsorbed CO species by hydrogen released from TiH_2.[7]

The second control experiment is the CO_2 methanation in the absence of external H_2 source and under otherwise identical conditions. As expected, despite the high intrinsic activity of RU NPs towards catalytic CO_2 hydrogenation,[65] no product is detected for Ru NPs due to absence of hydrogen (Fig. 6d). In contrast, TiH_2 shows a high H_2 production rate of 298.1 μmol h^{-1} $g_{cat.}^{-1}$, which is due to the release of hydrogen stored in TiH_2 and thus verifies the hydrogen storage and release capability of TiH_2.[28, 51] This explains why CO_2 can be reduced by TiH_2 even in the absence of external H_2 source. However, the negligible production rate of CH_4 and low selectivity of CH_4 over CO (denoted by the CH_4/CO rate ratio) indicate the poor intrinsic activity of TiH_2 towards catalytic CO_2 methanation. As compared with TiH_2, 100RTH delivers 22 times higher CH_4 production rate and 1.9 times higher CH_4 selectivity. These results, together with the results shown in Fig. 6a-c, collectively suggest that the Ru NPs in 100RTH are not only the predominant sites for CO_2 adsorption but also the predominant catalytic sites for CO_2 methanation. We further note that the CH_4 selectivity of 100RTH in the absence of H_2 is much worse than that in presence of stoichiometric amount of H_2 (Fig. 6a), which should be to the limited amount and very low partial pressure of H_2 released from TiH_2.[66]

Based on all the above discussion, we propose a plausible relationship between structure, MSI and catalytic performance of *m*RTH (Scheme 1). As well demonstrated in literature, the activation of carbonyl and hydrogen plays a critical role in efficient CO_2 methanation.[7, 8, 16] The carbonyl with partially positively charged C atoms in CO_2 and $Ru(CO)_n$ intermediates can be activated by directing electron transfer from support to Ru NPs, which is beneficial for carbonyl to get electrons from electron-enriched Ru NPs and thus to be easily stabilized for subsequent conversion into CH_4. Moreover, although hydrogen activation can be readily achieved on Ru NPs through spillover effect, excess Ru NPs should be avoided, since intense hydrogen spillover effect can be induced, which inversely leads to deteriorative catalytic activity towards CO_2 methanation by strengthening the adsorption of H_2O molecules and hindering the removal of H_2O molecules from catalyst surfaces.[16] Accordingly, the interfacial charge transfer and Hydrogen spillover effect should be well regulated for optimal catalytic activity. In our *m*RTH, benefitting from the TiO_xH_y surface layer on TiH_2 and the direct Ru–TiO_xH_y contact in 50- and 100RTH, notable electron transfer from Ti to Ru can be achieved under mild synthetic condition (Fig. 4), which enriches the electron on Ru NPs and thus facilitate the carbonyl activation for efficient CO_2 methanation. Meanwhile, the low to moderate Ru loading in 50- and 100RTH allows favourable hydrogen spillover effect (positively corelated to the Ru loading) for efficient CO_2 methanation by hydrogen activation. Therefore, the electron transfer and hydrogen spillover effect in 50- and 100RTH collectively contribute to the superior catalytic activity towards efficient CO_2 methanation. By comparison, the higher loading Ru NPs with partially indirect Ru–TiO_xH_y contact in 150- and 200RTH induces less sufficient Ti–Ru electron transfer for carbonyl activation, and disadvantageous hydrogen spillover effect due to the enhanced adsorption of H_2O molecules on catalyst surface, which in turn results in their much lower activity towards CO_2 methanation.

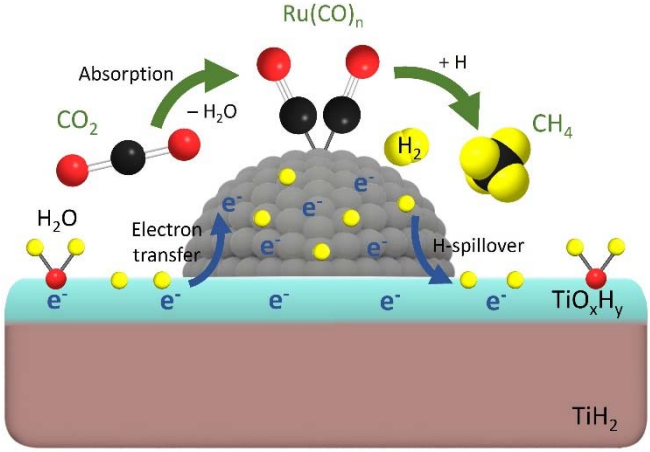

Scheme 1. Proposed relationship between structure, MSI and catalytic performances of *m*RTH towards CO_2 methanation.

Conclusions

In conclusion, we have developed a new heterogeneous catalyst of TiH_2-supported Ru NPs for highly efficient CO_2 methanation. Benefitting from the highly active, negatively charged hydrogen species of H^- in TiH_2, the TiH_2-supported Ru NPs show usual charge transfer from support to Ru NPs, which has not been achieved in the traditional TiO_2-supported Ru catalysts synthesized under similar mild conditions. Instead, TiH_2-supported Ru NPs show charge transfer behaviour similar to that in SMSI-mediated TiO_2–Ru catalysts prepared under high temperature reduction conditions. Moreover, as compared with SMSI-mediated TiO_2–Ru catalysts, the far milder synthetic condition for TiH_2-supported Ru NPs avoids the formation of adverse oxide overlayer on Ru NPs, which leads to the remarkably enhanced activation of CO intermediates on the TiH_2-supported, electron-enriched and efficiently exposed Ru NPs. Meanwhile, H_2 can also be activated by TiH_2-supported Ru NPs via hydrogen spillover effect, inevitably accompanied by the adverse hydration of catalyst surface. The electron transfer behaviour and hydrogen spillover effect are readily regulated by tuning the Ru loading, and a moderate Ru loading of 9.8 wt.% in 100RTH is optimized, in which the impacts of Ru loading on CO intermediate activation, H_2 activation and catalyst surface hydration are synergistically balanced. When evaluated at a low reaction temperature of 200 °C and under 4 bar pressure, 100RTH is capable of delivering a notable CH_4 selectivity of 99.8% and a remarkable CH_4 production rate of 168.7 mmol h^{-1} g_{Ru}^{-1}, which is 21.1 times more active than pure Ru NPs. Our work thus opens up a new avenue for the development of advanced

heterogeneous catalysts for the efficient conversion of CO_2 into value-added chemicals.

Author Contributions

The manuscript was written through contributions of all authors. All authors have given approval to the final version of the manuscript.

Conflicts of interest

There are no conflicts to declare.

Acknowledgements

This work was financially supported by the NSF (2021A1515010098), DST (STKJ202209075), CCE LAB (2111005) of Guangdong Province, the NKRD Program of China (2021YFA1500401), the NNSF of China (21821003, 21890380) and the LIRT Project of Guangdong PRTP (2017BT01C161).

Notes and references

1. T. Zhao, Z. Yang, Y. Tang, J. Liu and F. Wang, *Energy & Fuels*, 2022, **36**, 6711.
2. S. Das, J. Perez-Ramirez, J. Gong, N. Dewangan, K. Hidajat, B. C. Gates and S. Kawi, *Chem. Soc. Rev.*, 2020, **49**, 2937.
3. C. Tang, Y. Zheng, M. Jaroniec and S. Z. Qiao, *Angew. Chem. Int. Ed.*, 2021, **60**, 19572.
4. C. Vogt, M. Monai, G. J. Kramer and B. M. Weckhuysen, *Nat. Catal.*, 2019, **2**, 188.
5. W. Wang, S. Wang, X. Ma and J. Gong, *Chem. Soc. Rev.*, 2011, **40**, 3703.
6. K. Li, B. Peng and T. Peng, *ACS Catalysis*, 2016, **6**, 7485.
7. J. Zhou, Z. Gao, G. Xiang, T. Zhai, Z. Liu, W. Zhao, X. Liang and L. Wang, *Nat. Commun.*, 2022, **13**, 327.
8. Y. Zhang, W. Yan, H. Qi, X. Su, Y. Su, X. Liu, L. Li, X. Yang, Y. Huang and T. Zhang, *ACS Catal.*, 2022, **12**, 1697.
9. J. C. Matsubu, S. Zhang, L. DeRita, N. S. Marinkovic, J. G. Chen, G. W. Graham, X. Pan and P. Christopher, *Nat. Chem.*, 2017, **9**, 120.
10. J. C. Matsubu, V. N. Yang and P. Christopher, *J. Am. Chem. Soc.*, 2015, **137**, 3076.
11. A. Parastaev, V. Muravev, E. Huertas Osta, A. J. F. van Hoof, T. F. Kimpel, N. Kosinov and E. J. M. Hensen, *Nat. Catal.*, 2020, **3**, 526.
12. G. Melaet, W. T. Ralston, C. S. Li, S. Alayoglu, K. An, N. Musselwhite, B. Kalkan and G. A. Somorjai, *J. Am. Chem. Soc.*, 2014, **136**, 2260.
13. X. Jia, X. Zhang, N. Rui, X. Hu and C.-j. Liu, *Appl. Catal. B: Environ.*, 2019, **244**, 159.
14. C. Vogt, E. Groeneveld, G. Kamsma, M. Nachtegaal, L. Lu, C. J. Kiely, P. H. Berben, F. Meirer and B. M. Weckhuysen, *Nat. Catal.*, 2018, **1**, 127.
15. J. Ashok, M. L. Ang and S. Kawi, *Catal. Today*, 2017, **281**, 304.
16. Y. Guo, S. Mei, K. Yuan, D.-J. Wang, H.-C. Liu, C.-H. Yan and Y.-W. Zhang, *ACS Catal.*, 2018, **8**, 6203.
17. Z. Luo, G. Zhao, H. Pan and W. Sun, *Adv. Energy Mater.*, 2022, **12**, 2201395.
18. Y. Li, Y. Zhang, K. Qian and W. Huang, *ACS Catal.*, 2022, **12**, 1268.
19. Y. Zhang, X. Yang, X. Yang, H. Duan, H. Qi, Y. Su, B. Liang, H. Tao, B. Liu, Chen, X. Su, Y. Huang and T. Zhang, *Nat. Commun.*, 2020, **11**, 3185.
20. X. Li, J. Lin, L. Li, Y. Huang, X. Pan, S. E. Collins, Y. Ren, Y. Su, L. Kang, X. Liu, Y. Zhou, H. Wang, A. Wang, B. Qiao, X. Wang and T. Zhang, *Angew. Chem. Int. Ed.*, 2020, **59**, 19983.
21. S. J. Tauster, S. C. Fung and R. L. Garten, *J. Am. Chem. Soc.*, 1978, DOI: 10.1021/ja00469a029,, 170.
22. Q. Fu and T. Wagner, *Surf. Sci.*, 2007, **601**, 1339.
23. A. M. Abdel-Mageed, D. Widmann, S. E. Olesen, I. Chorkendorff, J. Biskupek and R. J. Behm, *ACS Catal.*, 2015, **5**, 6753.
24. M. Liu, Y. Yi, L. Wang, H. Guo and A. Bogaerts, *Catalysts*, 2019, **9**, 275.
25. Q. Wu, C. Zhang, M. Arai, B. Zhang, R. Shi, P. Wu, Z. Wang, Q. Liu, K. Liu, W. Lin, H. Cheng and F. Zhao, *ACS Catal.*, 2019, **9**, 6425.
26. T. Nakao, T. Tada and H. Hosono, *J. Phys. Chem. C*, 2019, **124**, 1529.
27. S. Samal, S. Cho, D. W. Park and H. Kim, *Thermochim. Acta*, 2012, **542**, 46.
28. C. Wang, L. Pan, Y. Zhang, S. Xiao and Y. Chen, *Int. J. Hydrogen Energy*, 2016, **41**, 14836.
29. D. Mandrino, I. Paulin and S. D. Škapin, *Mater. Characterization*, 2012, **72**, 87.
30. D. Wang, B. Kowalczyk, I. Lagzi and B. A. Grzybowski, *J. Phys. Chem. Lett.*, 2010, **1**, 1459.
31. D. Wang, B. Tejerina, I. Lagzi, B. Kowalczyk and B. A. Grzybowski, *ACS Nano*, 2010, **5**, 530.
32. S. Chen, W. Wang, X. Li, P. Yan, W. Han, T. Sheng, T. Deng, W. Zhu and H. Wang, *J. Energy Chem.*, 2022, **66**, 576.
33. I. Paulin, Č. Donik, D. Mandrino, M. Vončina and M. Jenko, *Vacuum*, 2012, **86**, 608.
34. Y. Zhang, C. Wang, Y. Liu, S. Liu, S. Xiao and Y. Chen, *Appl. Surf. Sci.*, 2017, **410**, 177.
35. G. Zhou, Y. Dong and D. He, *Appl. Surf. Sci.*, 2018, **456**, 1004.
36. J.-L. Liu, L.-J. Zhu, Y. Pei, J.-H. Zhuang, H. Li, H.-X. Li, M.-H. Qiao and K.-N. Fan, *Appl. Catal. A: General*, 2009, **353**, 282.
37. G. Zhou, H. Wang, J. Tian, Y. Pei, K. Fan, M. Qiao, B. Sun and B. Zong, *ChemCatChem*, 2018, **10**, 1184.
38. F. Su, F. Y. Lee, L. Lv, J. Liu, X. N. Tian and X. S. Zhao, *Adv. Funct. Mater.*, 2007, **17**, 1926.
39. X. D. Wang, Y. H. Huang, J. F. Liao, Y. Jiang, L. Zhou, X. Y. Zhang, H. Y. Chen and D. B. Kuang, *J. Am. Chem. Soc.*, 2019, **141**, 13434.
40. Y. Liu, Y. Li, F. Peng, Y. Lin, S. Yang, S. Zhang, H. Wang, Y. Cao and H. Yu, *Appl. Catal. B: Environ.*, 2019, **241**, 236.
41. M. A. Amin, S. A. Fadlallah, G. S. Alosaimi, E. M. Ahmed, N. Y. Mostafa, P. Roussel, S. Szunerits and R. Boukherroub, *ACS Appl. Mater. Interfaces*, 2017, **9**, 30115.
42. W. Lisowski, A. van den Berg, H. J, D. Leonard and H. J. Mathieu, *Surf. Interface Anal.*, 2020, **29**, 292.
43. C. Wang, Y. Zhang, Y. Wei, L. Mei, S. Xiao and Y. Chen, *Powder Technol.*, 2016, **302**, 423.
44. Z. Zhou, J. Li and Z. You, *Appl. Surf. Sci.*, 2022, **587**, 152856.
45. M. Xu, S. Yao, D. Rao, Y. Niu, N. Liu, M. Peng, P. Zhai, Y. Man, L. Zheng, B. Wang, B. Zhang, D. Ma and M. Wei, *J. Am. Chem. Soc.*, 2018, **140**, 11241.

46. A. Mahdavi-Shakib, K. B. S. Kumar, T. N. Whittaker, T. Xie, L. C. Grabow, R. M. Rioux and B. D. Chandler, *Angew. Chem. Int. Ed.*, 2021, **60**, 7735.
47. A. Gankanda, D. M. Cwiertny and V. H. Grassian, *J. Phys. Chem. C*, 2016, **120**, 19195.
48. Z. Wang, H. Wang, X. Wang, X. Chen, Y. Yu, W. Dai, X. Fu and M. Anpo, *J. Phys. Chem. C*, 2021, **125**, 3242.
49. M. Y. Aslan and D. Uner, *Int. J. Hydrogen Energy*, 2019, **44**, 18903.
50. A. R. Kennedy and V. H. Lopez, *Mater. Sci. Engineering: A*, 2003, **357**, 258.
51. V. Bhosle, E. G. Baburaj, M. Miranova and K. Salama, *Mater. Sci. Engineering: A*, 2003, **356**, 190.
52. M. Ma, L. Wang, Y. Wang, W. Xiang, P. Lyu, B. Tang and X. Tan, *J. Alloys Compounds*, 2017, **709**, 445.
53. B. Matijasevic-Lux, J. Banhart, S. Fiechter, O. Görke and N. Wanderka, *Acta Mater.*, 2006, **54**, 1887.
54. W. Karim, C. Spreafico, A. Kleibert, J. Gobrecht, J. VandeVondele, Y. Ekinci and J. A. van Bokhoven, *Nature*, 2017, **541**, 68.
55. R. Prins, *Chem. Rev.*, 2012, **112**, 2714.
56. W. C. Conner and F. J. L, *Chem. Rev.*, 1995, **95**, 759.
57. C. Mao, J. Wang, Y. Zou, G. Qi, J. Y. Yang Loh, T. Zhang, M. Xia, J. Xu, F. Deng, M. Ghoussoub, N. P. Kherani, L. Wang, H. Shang, M. Li, J. Li, X. Liu, Z. Ai, G. A. Ozin, J. Zhao and L. Zhang, *J. Am. Chem. Soc.*, 2020, **142**, 17403.
58. N. Daelman, M. Capdevila-Cortada and N. Lopez, *Nat. Mater.*, 2019, **18**, 1215.
59. H. L. Tang, Y. Su, B. Z. Zhang, A. F. Lee, M. A. Issac, K. Wilson, L. Li, Y. Ren, J. Huang, H. Masatake, B. Qiao, X. Liu, C. Jin, D. S. Su, J. Wang and T. Zhang, *Sci. adv.*, 2017, **3**, 1700231.
60. K. M. Jesús Graciani, Fang Xu, Ashleigh E. Baber, Jaime Evans, Sanjaya D. Senanayake, Darío J. Stacchiola, Ping Liu, Jan Hrbek, Javier Fernández Sanz, José A. Rodriguez, *Science*, 2014, **345**, 6196.
61. B. H. Solis, Y. Cui, X. Weng, J. Seifert, S. Schauermann, J. Sauer, S. Shaikhutdinov and H. J. Freund, *Phys. Chem. Chem. Phys.*, 2017, **19**, 4231.
62. L. Liu, C. Zhao and Y. Li, *J. Phys. Chem. C*, 2012, **116**, 7904.
63. M. Pachecka, J. M. Sturm, C. J. Lee and F. Bijkerk, *J. Phys. Chem. C, Nanomater. Interfaces*, 2017, **121**, 6729.
64. P. Zhao, Y. He, X. Wen and H. Jiao, *Surf. Sci.*, 2022, **715**, 121936.
65. K. R. Thampi, J. Kiwi and M. Gratzel, *Nature*, 1987, **327**, 506.
66. M. S. Frei, M. Capdevila-Cortada, R. García-Muelas, C. Mondelli, N. López, J. A. Stewart, D. Curulla Ferré and J. Pérez-Ramírez, *J. Catal.*, 2018, **361**, 313.

Table of Contents (ToC)

TiH_2-support Ru catalyst is developed for highly efficient CO_2 methanation, in which usual support-to-metal electron transfer behaviour and hydrogen spillover effect are synergistically regulated to balance CO intermediate activation, H_2 activation and catalyst surface hydration.

ToC Figure